Measurement 185 (2021) 110006

Contents lists available at ScienceDirect

Measurement

journal homepage: www.elsevier.com/locate/measurement

Design of a milli-newton force balance for hypersonic rarefied wind tunnel

Chen-Wu Wu [a,*], Cong Liu [a,b], Deng-Liang Hu [a], Hong-Li Liu [a], He-Ji Huang [a,*]

[a] Institute of Mechanics, Chinese Academy of Sciences, Beijing 100190, China
[b] School of Engineering Science, University of Chinese Academy of Sciences, Beijing 100049, China

ARTICLE INFO

Keywords:
Strain
Balance
Milli-newton
Design
Calibration

ABSTRACT

A multi-axial balance based on strain gauge was designed to measure the milli-newton gas-dynamic forces. The static and dynamic characteristics of the balance were analyzed by numerical method. The strain responses of the structure to static as well as transient loading were maintained by finite element analysis and the measuring capacity estimated. The quasi-static calibration was carried through with standard weights and the sensitivity coefficient obtained. Tentative experiments were conducted in a hypersonic rarefied wind tunnel and typical outcomes were demonstrated as preliminary validation of the design.

1. Introduction

The measurements of small forces attract a great many of designing and research for the widely applications [1,2], of which a few could be named herein in the field of micro systems as an example. A three-axis force sensor was developed by M. Horie et al. for the microhandling systems that involves load level up to 1 N [3], a high precision torque sensor with capacitive probe was designed by B.-M. Finio et al. for microrobotics application [4] and A. Suhariyono et al. designed a balance of measuring capacity about 10 Newton to investigate the aerodynamic characteristics of a micro aerial vehicle [5]. A test stand of test capacity of about 100 milli-newton was designed by D. Mueller et al. to measure the thrust and lift forces for a micro air vehicle [6] and a mechanical microbalance was used by S. Shkarayevto et al. to investigate the small aerodynamic forces and moments acted on the wings of a locust under test in a wind tunnel [7].

Actually, there're also a great many successful cases in the biomedical area [8]. Peter J. Berkelman et al. designed a high-resolution force sensor as steady-hand assistance in various eye and ear microsurgical procedures [9]. D. Ye et al. designed a force sensor to monitor the small force of magnitude at the order of mN to avoid the damage to blood vessel during surgical procedures [10]. B.-W. Quist et al. built a wire-form sensor of resolution up to 0.02mN to measure the force results from rat whisker sweeping against an object [11]. An ultra-sensitive force sensor based on optical measurement was designed by J. Rajagopalan et al. to describe very small forces less than 1 μm newton in biological studies [12] and a tri-axial force sensor by embedding the piezoresistive silicon nanowires in elastic parts developed by W.-T. Park to detect the force acted on the guide-wire within a vascular vessel during surgical procedures [13].

Although the very fine forces have been well measured in these biomedical applications, it is not the case for many other engineering objectives. For instance, the small force measurement in the hypersonic rarefied wind tunnel (HRWT) always requires the instrument to be accurate as well as robust enough. T. Ozawa et al. reported a series of work on the aerodynamic characteristic of model in HRWT, in which the DSMC simulations were particularly discussed and the models of sphere/ aero-shell suspended by a string/ wire were successfully investigated [14,15,16,17]. N. Rembaut, et al. also revealed the big challenge in experimental measurements in such environment [18], although a great many integrated balances have been developed for the aerodynamic measurement for other low speed or high speed wind tunnel [19,20,21,22].

This article presents briefly the concept design and preliminary test of a five-component micro balance to be applied to aerodynamic measurement for hypersonic rarefied wind tunnel. The mechanical responses of the basic part of the balance to static as well as dynamic loadings are analyzed and the linearity deviation is discussed, by which the origin idea is validated.

2. Structure configuration

The fundamental structure is sketched in Fig. 1, which mainly involves a cruciform-section beam and a simple thin plate beam. There only exists a thin layer of dimensions $S_{HV} \times W_{HV} \times t_{HV}$ at every measuring location to reduce locally the deflection stiffness of the

* Corresponding authors at: No.15 Beisihuan Xi Road, Haidian District, Beijing 100190, China.
E-mail addresses: chenwuwu@imech.ac.cn (C.-W. Wu), huang@imech.ac.cn (H.-J. Huang).

https://doi.org/10.1016/j.measurement.2021.110006
Received 12 May 2021; Received in revised form 1 July 2021; Accepted 8 August 2021
Available online 24 August 2021

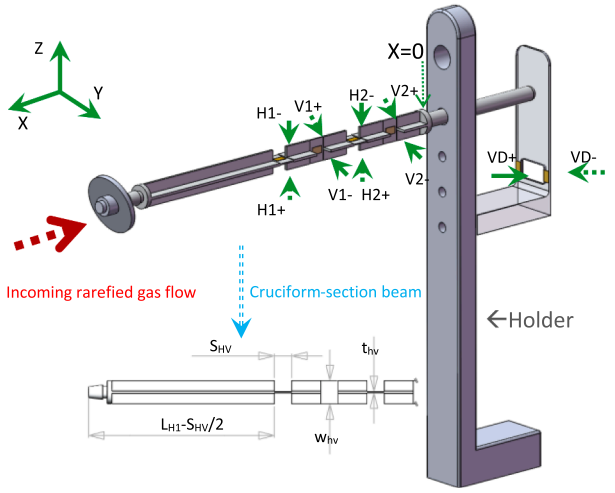

Fig. 1. Structural configuration.

cruciform-section beam. Such treatment could keep the overall deflection stiffness of the cruciform-section beam and avoid large displacement of the frontend of the cruciform-section beam. Similarly, the effective width is reduced by removing the material in the central region only at the measuring position for the vertical plate beam. The dimensions have been listed in Table 1 for the sake of simplification.

The axial direction is represented by X, which is parallel to the drag component acted on the model. The horizontal direction is represented by Y parallel to the lateral force and the vertical direction is represented by Z parallel to the lift component.

According to beam theory [23,24], the drag component F_X would be proportionally related to the strain ε_{zz}^D at the location of *VD* in Fig. 1 by the following equation

$$\varepsilon_{zz}^D = \frac{F_X l_D t_D}{2EI_{zz}^D} \tag{1}$$

with l_D being the arm of the drag force relative to the measuring location at the vertical strip beam, E the Young's modulus and

$$I_{zz}^D = \frac{W_D t_D^3}{12} \tag{2}$$

Wherein, W_D and t_D are the effective width and thickness of the measurement position, respectively.

Therefore, the drag component F_X could be written as

$$F_X = \varepsilon_{zz}^D \frac{2EI_{zz}^D}{l_D t_D}. \tag{3}$$

Generally speaking, the drag component is large in comparison to the other component and would not be discussed in more detail in this work. The components of lift force F_Z, lateral force F_Y, pitching moment M_Y and yawing moment M_Z could be obtained by measuring the elastic strains ε_{XX}^{H1}, ε_{XX}^{H2}, ε_{XX}^{V1} and ε_{XX}^{V2} at locations of *H1*, *H2*, *V1* and *V2*. Theoretically, we have the following relationships if contemporarily ignore the small quantities of high orders resulted from axial compression, torsion or geometrical deviations.

$$\begin{pmatrix} \varepsilon_{XX}^{H1} \\ \varepsilon_{XX}^{H2} \\ \varepsilon_{XX}^{V1} \\ \varepsilon_{XX}^{V2} \end{pmatrix} = \mathrm{T} \begin{pmatrix} M_Y \\ F_Z \\ M_Z \\ F_Y \end{pmatrix} \tag{4}$$

And the ideal coefficient matrix is

$$\mathrm{T} = \begin{bmatrix} \frac{t_{HV}}{2EI_{YY}^H} & -\frac{t_{HV} l_{H1}}{2EI_{YY}^H} & 0 & 0 \\ \frac{t_{HV}}{2EI_{YY}^H} & -\frac{t_{HV} l_{H2}}{2EI_{YY}^H} & 0 & 0 \\ 0 & 0 & -\frac{t_{HV}}{2EI_{zz}^V} & -\frac{t_{HV} l_{V1}}{2EI_{ZZ}^V} \\ 0 & 0 & -\frac{t_{HV}}{2EI_{ZZ}^V} & -\frac{t_{HV} l_{V2}}{2EI_{ZZ}^V} \end{bmatrix} \tag{5}$$

For the case that the strain gages are stalled at the ideal central region at every measuring position. The symbol t_{HV} is the effective thickness of beam at the measuring location. The force arms of l_{H1}, l_{H2}, l_{V1} and l_{V2} are in corresponding to the locations of *H1*, *H2*, *V1* and *V2* in sequence, as roughly denoted in Fig. 1. The moments of inertia are

$$I_{YY}^H = I_{ZZ}^V = \frac{W_{HV} t_{HV}^3}{12} \tag{6}$$

To be noted, the normal strains of the two sides at any test location of *H1*, *H2*, *V1* and *V2* would be almost of identical absolute magnitude with opposite directional sign. Hence, a pair of semiconductor strain gages would be stalled symmetrically at the two sides of the thin plate beam at the position H1, H2, V1 and V2. The apparent strain could be doubled by connecting the two strain gages at the opposite sides of the thin beam into a half Wheatstone bridge at every test position of H1, H2, V1 and V2.

The lift force F_Z, lateral force F_Y, pitching moment M_Y and yawing moment M_Z could be computed by the measured strains at the specific positions as

$$\begin{pmatrix} M_Y \\ F_Z \\ M_Z \\ F_Y \end{pmatrix} = \mathrm{T}^{-1} \begin{pmatrix} \varepsilon_{XX}^{H1} \\ \varepsilon_{XX}^{H2} \\ \varepsilon_{XX}^{V1} \\ \varepsilon_{XX}^{V2} \end{pmatrix} \tag{7}$$

Of course, the practical coefficient matrix could be calibrated by simple static experiments. The dependency of the coefficients on the omitted small quantities might be involved and matrix T might include more non-zero elements.

3. Static and dynamic analysis

3.1. Description on the finite element model

The finite element model was set up for the cruciform-section beam

Table 1
Geometrical parameters.

Variable	W_{HV}	t_{HV}	S_{HV}	l_{H1}	l_{H2}	l_{V1}	l_{V2}	l_B	R_D	t_D	θ_D
Value/mm	10	0.5	7.5	97.75	137.75	117.75	157.75	176.5	12.5	2	15°

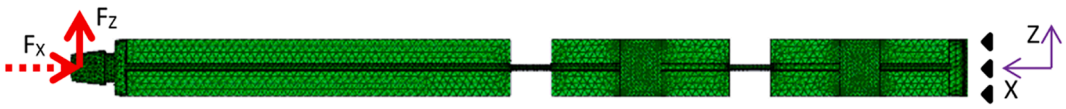

Fig. 2. Finite element model and load sketch.

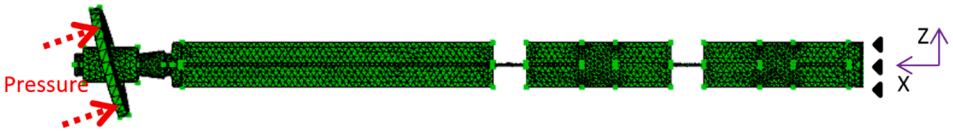

Fig. 3. Finite element model for dynamic loading analysis.

and the plate model of the balance as schematically shown in Figs. 2 and 3, considering the fact that such a novel structure could be the most susceptible part for the present balance. The elastic equations that dominate the deformation field of the balance beam are [23,24]:

$$(\lambda + G)\frac{\partial e}{\partial x_i} + G\nabla^2 u_i - \rho\frac{\partial^2 u_i}{\partial t^2} = 0, i = 1,2,3 \quad (8)$$

$$e = \frac{\partial u_i}{\partial x_i},\ \ i = 1,2,3 \quad (9)$$

$$\nabla^2 = \frac{\partial^2}{\partial {x_i}^2},\ \ i = 1,2,3 \quad (10)$$

Wherein, x_i, i = 1,2,3 represent the rectangular coordinates; u_i, i = 1,2,3 the components of displacements; $\lambda = \frac{\mu E}{(1+\mu)(1-2\mu)}$ and $G = \frac{E}{2(1+\mu)}$ with E being the modulus of elasticity and μ the Poisson's ratio.

The detailed geometrical parameters of the cruciform-section beam are listed in Table 1, in which l_B is the length measured from the front end of the beam to the constrained cross section. Moreover, R_D, t_D and θ_D are the radius, thickness and inclination angle of the disk model. Note that the real mesh of the geometry consists of 103523 tetrahedral elements.

The aluminum 6063-T83 was chosen and the Young's modulus and Poisson's ratio are 69GPa and 0.33, respectively [25]. The yield stress of this type of aluminum is not lower than 150 MPa according to the handbook [25], which indicates a yield strain about 2000με under uniaxial tension or compression resulted from bending.

The stationary response was achieved by solving the elastic static equations numerically by commercial finite element software, which could be expressed by (8), (9) and (10) by letting

$$\frac{\partial^2 u_i}{\partial t^2} = 0 \quad (11)$$

Moreover, the totally constrained condition on the cross-section (x = 0) adjacent to the holder the equations could be expressed as:

$$u_i = 0,\ I = 1,2,3 \text{ for } x = 0 \quad (12)$$

$$Fz = 1mN \text{ at } x = l_B \quad (13)$$

The static stability analysis was conducted on the balance with applying a unit axial compressive force, i.e. Fx = 1 N to the balance beam as denoted by the dotted arrow in Fig. 2, and the natural frequencies and mode vector could be obtained by solving the eigenvalue equation.

$$([K] + \lambda_i[S])\{\psi_i\} = 0 \quad (14)$$

wherein, [K] is the stiffness matrix of the structure, [S] is the structural geometric stiffness matrix under the unit input load, i.e. Fx = 1 N; λ_i represents the buckling load multipliers at the i^{th} rank of buckling mode and ψ_i the buckling mode vectors.

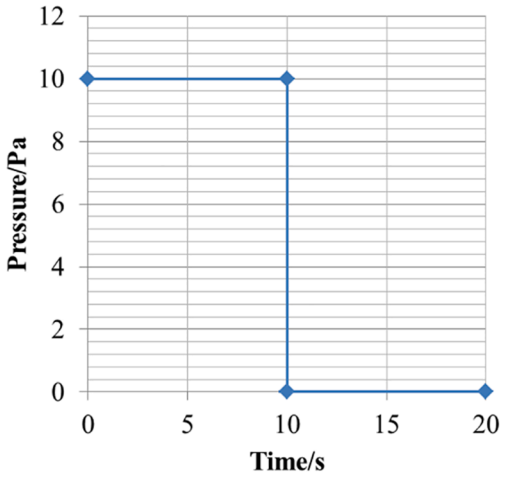

Fig. 4. The rectangle pulse of uniform pressure.

The dynamic response characteristic of the balance was obtained by solving the eq. (8) with a rectangle pressure load pulse of stable peak pressure 10 Pa and duration 10 s as shown in Fig. 4 being exerted at the forward face of the plate model as schematically shown in Fig. 3. Note that the real mesh of the computation domain consists of 130941 tetrahedral elements and the balance is assumed to be stationary before the abrupt loading.

The plate model is made up of an inclined annular plate of diameter 25 mm and a horizontal two-stage cylindrical bump. The inclination angle of the annular plate to the Z-axis is 15° and the annular plate is vertical to the plane XOZ. The thickness of the annular plate is 2 mm. The large and small diameters of the two-stage cylindrical bump are 8 mm and 5 mm, respectively. The height of the small cylinder is 2 mm and the average height of the large cylinder is about 5 mm.

3.2. The computational results and discussion

The static deformation of the balance subjected to the action of lift force of Fz = 1mN is computated firstly. The normal strain tensor at x direction is shown in Fig. 5, in which the apparent strain concentration could be found to be confined within the thin beam slabs at the positions of H1 and H2. Moreover, the average normal strain along axial direction at the top side and bottom side of the thin beam slab at position H1 are about −2.6904με and +2.6879με, respectively. The slight difference in absolute values of the strains at the two sides of the test position H1 should be due to the numerical error. Therefore, the theoretical sensitivity coefficient of the test point H1 to the lift component should be about 2.69με/mN. Considering the fact that the force arm of test position V2 is nearly twice that of H1, the theoretical limitation of measurement ability for the lateral force alone should approximately be 2000με/

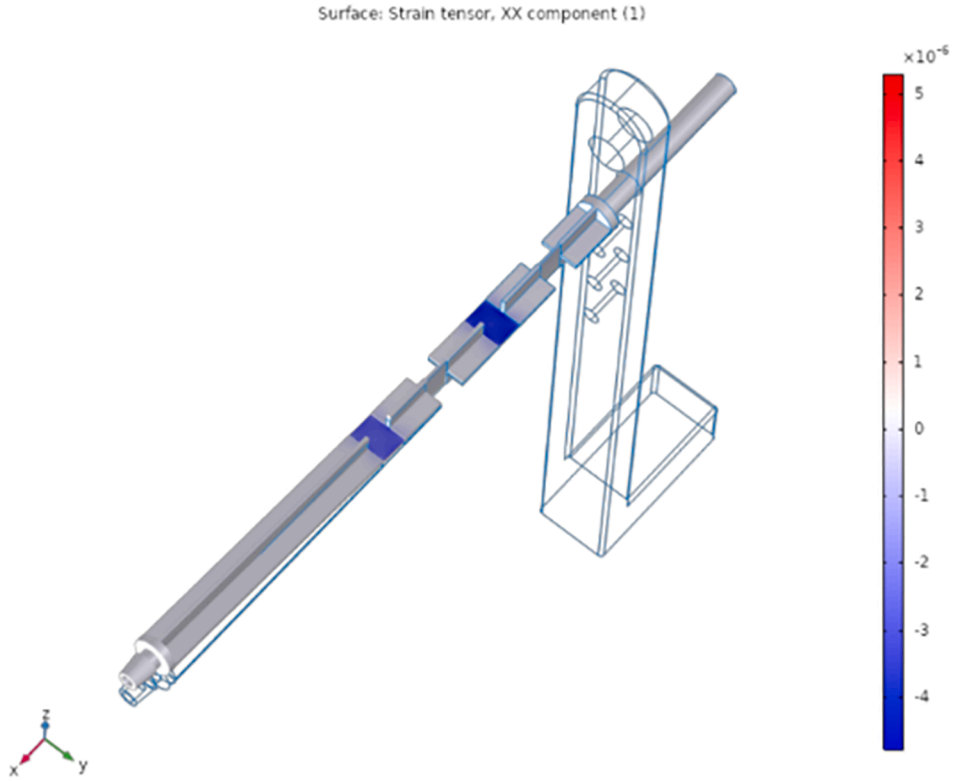

Fig. 5. The static strain contour in the cruciform-section beam under the action of $F_Z = 1$ mN.

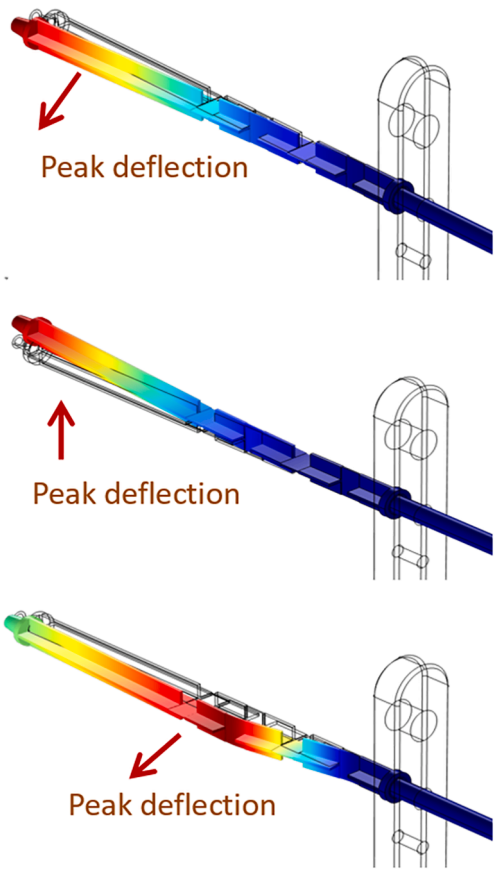

Fig. 6. Buckling modes of 1st, 2nd and 3rd order under the action of $F_X = 1$ N.

(2.69με/mN)/2≈370mN. Of course, the theoretical limitation for the lift force alone should be slightly higher than 370mN due to the slightly shorter force arm of H2 in comparison to V2.

Then, the stability analysis was conducted on the balance beam. The three lower buckling modes are shown in Fig. 6 with the critical load factors of about 4.2, 5.1 and 57.3 in sequence, which means that the axial force should be less than 4.2 N to maintain the stability of the balance. Such stability condition could be fully met by the experimental environment within the hypersonic rarefied wind tunnel, in which the maximum axial force acted upon a model aircraft with frontal area 0.01 m^2 is only 0.1 N for the cases of peak dynamic pressure about 10 Pa.

Finally, the transient responses of the system were obtained by solving the dynamic equations (8), (9) and (10) numerically by the finite element method and the dynamic strain oscillation at the test location H1 is diagramed in Fig. 7.

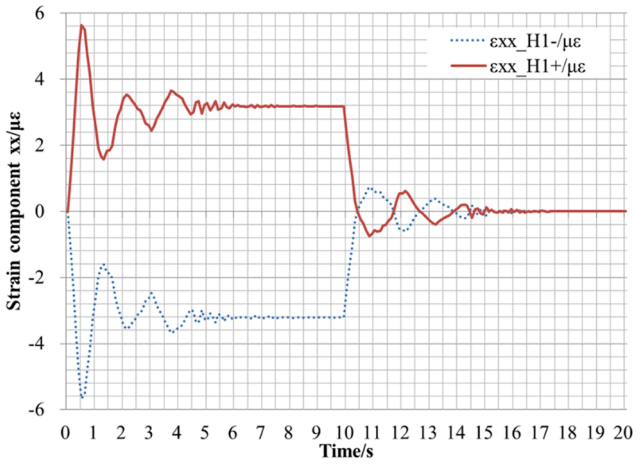

Fig. 7. Dynamic characteristic of the strain at position H1.

Table 2
Weights and loading combinations.

Weight size			5 mg	10 mg	20 mg	50 mg	100 mg	200 mg	500 mg
Loading combinations	Small range	1st	×1						
		2nd	×1	×1					
		3rd	×1	×1	×1				
		4th	×1	×1	×2				
		5th	×1	×1	×2	×1			
	Large range	1st					×1		
		2nd					×1	×1	
		3rd					×1	×2	
		4th					×1	×2	×1

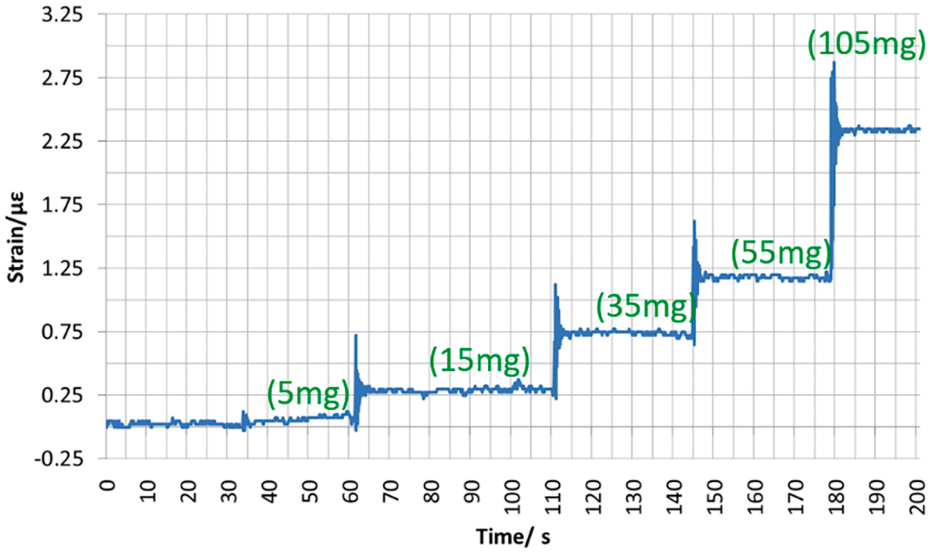

Fig. 8. Typical calibration outcome for small load force range.

The effective lift force acted on the model by the pressure is about 1.1906mN according to the product of effective projective area, 460 mm^2 × sin(15°) and pressure, 10 Pa and the effective moment is zero due to the symmetrical characteristic of the configuration and loading. The stable normal strain at the measuring position is about 3.2με, which is about 1.1896 times the strain induced by 1mN lift as shown in Fig. 5. The relative error is about 8.4e-4, which is less than 0.1%. From this point of view, one can say that the static and dynamic results are in consistent with each other. The strain history at the measuring point shown in Fig. 7 also indicates that the transient would decay in short time and stationary state be restored again after a load is abruptly applied in the initially rest state.

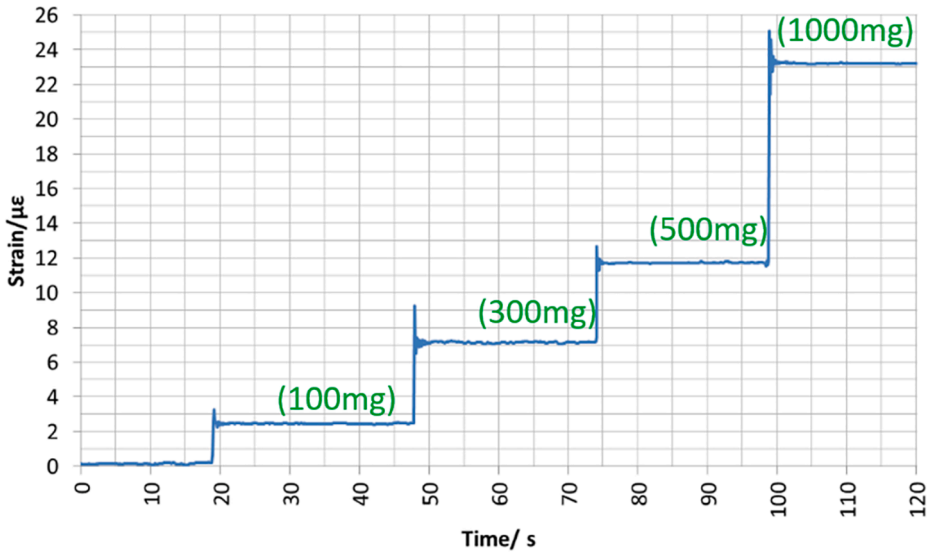

Fig. 9. Typical calibration outcome for large load force range.

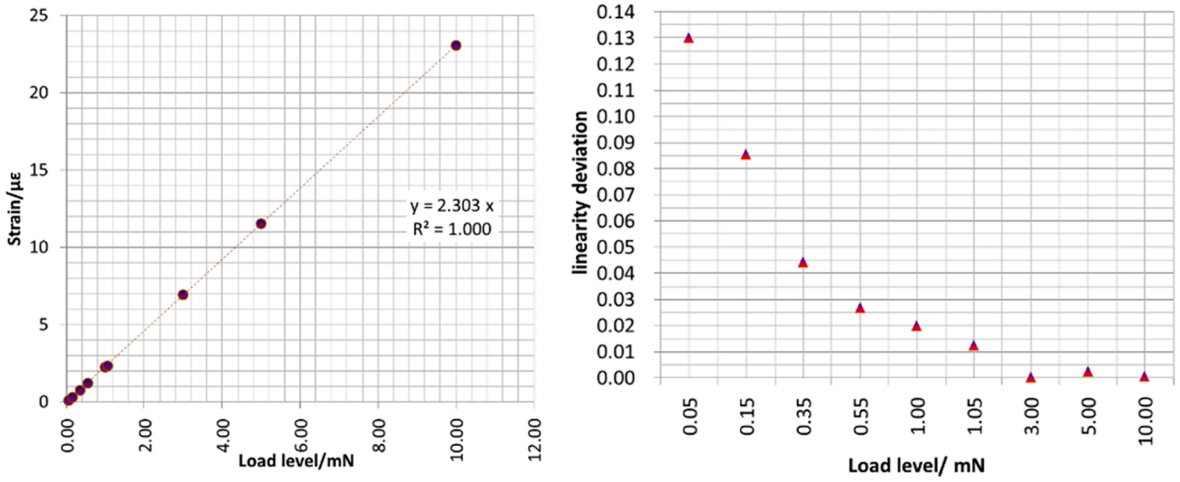

Fig. 10. Linearity and its deviation of the responses of the balance to the load.

4. Calibration and tentative experiment

The standard slice weights are used to load at the frontend of the cruciform-section beam and, the Si-based semiconductor strain gages (KSN-2-120 series) are installed at the measuring positions to sense the elastic strain therein. The outcomes of the measuring location of lowest sensitivity, i.e. H1 are extremely discussed in this article to ensure generality. The sizes of the slice weights and the loading tactics for the calibration of both small range and large range are listed in Table 2.

The typical calibration test results are shown in Figs. 8 and 9 for relatively small range and large range of the applied force, respectively.

It is also indicated in Fig. 8 that the recovery time for the balance to return stable is slightly shorter than the theoretical prediction as shown in Fig. 7. Although, it looks like that the recovery time becomes much shorter when the applied forces are greater than 100 mg as shown in Fig. 9, which might have been induced by the visual error as the absolute is large in comparison to the small fluctuation with time.

The linearity and its deviation of the responses of the balance to the loading is demonstrated in Fig. 10, in which the abscissa is the load level and ordinate the measured value.

One can see that good linearity is revealed by the calibration curves in Fig. 10. The real sensitivity coefficient could be calculated to be about 2.30με/mN according to the slope of the calibration line in Fig. 10. It is noteworthy that the value R^2 equals to 1 with three-digit precision, which means a perfect linearity of the data. One could quickly notice that the real sensitivity coefficient, 2.30με/mN is less than the theoretical one, 2.69με/mN by 14.5%, which might be due to the geometrical deviation resulted from machining error and the local stiffness alteration resulted from the installation of strain gages. Basically, the linearity error would decrease quickly with the increasing of the load level. In detail, the linearity error would be greater than 10% if the load level is lower than 0.1mN. The linearity error would be less than 5% if the load level is higher than 0.5mN and the error would be less than 2% were the load level is higher than 1mN.

The in-situ experiment was carried through in a hypersonic rarefied wind tunnel as shown in Fig. 11. The configuration of the model and the geometrical relationship are identical to that as shown in Fig. 1. The diameter of the uniform region of the incoming flow is about 20 mm, the incoming nitrogen flow velocity is about 5 km/s and the order of magnitude of the nitrogen density is known to be $\sim 10^{-5}$ kg/m^3.

A typical test result is plotted in Fig. 12, for which the mass flow rates are about 0.025 g/s, 0.050 g/s, 0.075 g/s, 0.100 g/s and 0.125 g/s in sequence. The measured lift components indicate that the pressure applied to the model by the incoming flow does not accurately relate linearly to the volumetric flow rate. Moreover, there is negative lift

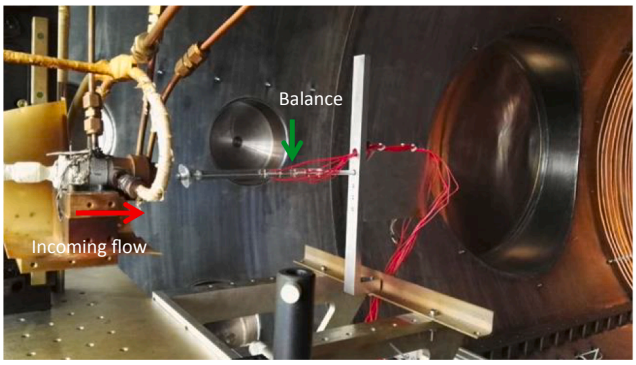

Fig. 11. In-situ experiment in the hypersonic rarefied wind tunnel.

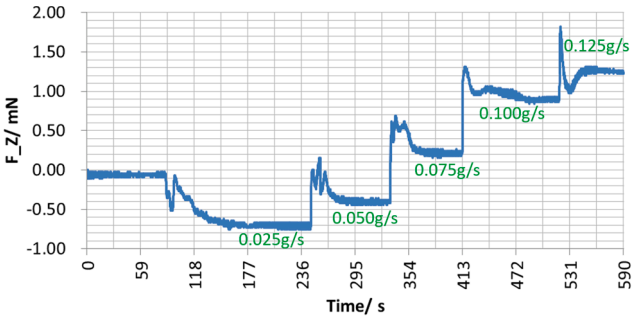

Fig. 12. Typical measured lift for the plate model in the rarefied gas tunnel.

acted on the model when the volumetric flow rate is small, like as the two cases of 0.025 g/s and 0.050 g/s as shown in Fig. 12. Such abnormal phenomena should have been due to the complicated interaction between the front geometry and the incoming flow. It is also revealed that the recovery time would decrease with the increase of mass flow rate of the incoming flow and there are always not reverse overshooting due to the real viscosity characteristic in the flow field.

5. Summary

A strain micro-balance was designed for measurement of millinewton gas dynamic forces. Static as well as dynamic responses of the balance to the loading were analyzed based on finite element model. The critical axial force to induce the instability of the cruciform-section

beam is about 4.2 Newton. The theoretical least sensitivity of the micro-balance is about 2.69με/mN in its current configuration while the real one is about 2.30με/mN. Preliminary test in the hypersonic rarefied wind tunnel justify the compatibility of the balance to the environment and the ability to measure small aerodynamic forces acted on the target model.

CRediT authorship contribution statement

Chen-Wu Wu: Conceptualization, Methodology, Investigation, Writing – original draft, Writing – review & editing, Funding acquisition. **Cong Liu:** Validation, Formal analysis, Visualization. **Deng-Liang Hu:** Validation, Software. **Hong-Li Liu:** Validation, Investigation. **He-Ji Huang:** Investigation, Resources, Writing – review & editing, Project administration, Funding acquisition.

Declaration of Competing Interest

The authors declare that they have no known competing financial interests or personal relationships that could have appeared to influence the work reported in this paper.

Acknowledgements

This work was supported by the Strategic Priority Research Program of Chinese Academy of Sciences (Grant No. XDA17030100, XDA17030100200).

References

[1] Y. Wei, Q. Xu, An overview of micro-force sensing techniques, Sens. Actuat. A 234 (2015) 359–374.
[2] J. Zhu, T. Hayashi, A. Nishino, K. Ogushi, Development of 2 N dead-weight type force standard machine, Measurement 154 (2020), 107463.
[3] M. Horie, H. Funabashi, K. Ikegami, A study on micro force sensors for microhandling systems, Microsyst. Technol. 1 (3) (1995) 105–110.
[4] B.M. Finio, K.C. Galloway, R.J. Wood, An ultra-high precision, high bandwidth torque sensor for microrobotics applications, IEEE (2011) 31–38.
[5] Arief Suhariyono, Jong Hyun Kim, Nam Seo Goo, Hoon Cheol Park, Kwang Joon Yoon, Design of precision balance and aerodynamic characteristic measurement system for micro aerial vehicles, Aerospace Sci. Technol. 10 (2006) 92–99.
[6] D. Mueller, H.A. Bruck, S.K. Gupta, Measurement of thrust and lift forces associated with drag of compliant flapping wing for micro air vehicles using a new test stand design, Exp. Mech. 50 (6) (2010) 725–735.
[7] S. Shkarayev, R. Kumar, Instantaneous forces in locust flapping wings, 32nd AIAA Appl. Aerodyn. Conference (2014) 1–21.
[8] Mehmet Engin, Alparslan Demirel, Erkan Zeki Engin, Musa Fedakar, Recent developments and trends in biomedical sensors, Measurement 37 (2005) 173–188.
[9] Peter J. Berkelman, Louis L. Whitcomb, Russell H. Taylor, and Patrick Jensen, A miniature instrument tip force sensor for robot/human cooperative microsurgical manipulation with enhanced force feedback, in S.L. Delp, A.M. DiGioia, and B. Jaramaz (Eds.): MICCAI (2000): 897-906.
[10] D. Ye, H. Mozaffari-Naeini, C. Busart, N.V. Thakor, MEMSurgery: an integrated test-bed for vascular surgery, Med. Robot. Comput. Assist. Surgery 01 (03) (2005) 21, https://doi.org/10.1581/mrcas.2005.010313.
[11] B.W. Quist, M.J.Z. Hartmanna, A two-dimensional force sensor in the millinewton range for measuring vibrissal contacts, J. Neurosci. Methods 172 (2008) 158–167.
[12] J. Rajagopalan, A. Tofangchi, M. Taher, A. Saif, Highly linear, ultra sensitive bio-mems force sensors with large force measurement range, IEEE (2010) 88–91.
[13] Woo-Tae Park, Rama Krishna Kotlanka, Liang Lou, Muhammad Hamidullah, Chengkuo Lee, MEMS tri-axial force sensor with an integrated mechanical stopper for guidewire applications, Microsyst Technol (2013) 19:1005-1015.
[14] T.S. Ozawa, K. Fujita, Experimental and numerical studies of hypersonic flows in the rarefied wind tunnel, 10th AIAA/ASME J. Thermophys. Heat Transfer (2010) 1–15.
[15] Toshiyuki Suzuki1, Takashi Ozawa and Kazuhisa Fujita, Aerodynamic Characteristics Evaluation Under Hypersonic Rarefied Flow Conditions, 44th AIAA Thermophysics Conference, 2013.
[16] T. Ozawa, T. Suzuki, K. Fujita, Aerodynamic Measurements and computational analyses in hypersonic rarefied flows, AIAA J. 53 (11) (2015) 3327–3337.
[17] T. Ozawa, K. Fujita, T. Suzuki, Development of an aerodynamic measurement system for hypersonic rarefied flows, Rev. Sci. Instrum. 86 (015105) (2015) 1–11.
[18] N. Rembaut, R. Joussot, V. Lago, Aerodynamical behavior of spherical debris in the supersonic and rarefied wind tunnel MARHy, J. Space Saf. Eng. 7 (3) (2020) 411–419.
[19] B. Ilić, M. Miloš, J. Isaković, Cascade nonlinear feedforward-feedback control of stagnation pressure in a supersonic blowdown wind tunnel, Measurement 95 (2017) 424–438.
[20] B. Liu, S. Li, H. Gao, Z. Dai, X. Hong, Suspension force measuring system for hypersonic wind tunnel test: design and tests, Measurement 143 (2019) 226–233.
[21] S. Li, K. Li, B. Liu, H. Gao, Y.i. Sun, Z. Dai, W. Liu, A new dynamic modelling methodology of a force measuring system for hypersonic impulse wind tunnel, Measurement 164 (2020), 108012.
[22] K.-Y. Park, Y.-H. Sung, J.-H. Han, Development of a cable suspension and balance system and its novel calibration methods for effective wind tunnel tests, Measurement 170 (2021), 108717.
[23] L.D. Landau, E.M. Lifshitz, Theory of Elasticity (3rd edition), Butterworth Heinemann, 1999.
[24] S.P. Timoshenko, J.N. Goodier, Theory of Elasticity (3rd edition), McGraw-Hill companies, 2004.
[25] CAMH Editorial Committee, China Aeronautical Materials Handbook, Vol. 3 (2nd edition), Standards Press of China, 2002.